Bacterial infection imaging with [18F]fluoropropyl-trimethoprim

Mark A. Sellmyer[a,1], Iljung Lee[a], Catherine Hou[a], Chi-Chang Weng[a], Shihong Li[a], Brian P. Lieberman[a], Chenbo Zeng[a], David A. Mankoff[a], and Robert H. Mach[a,1]

[a]Department of Radiology, University of Pennsylvania, Philadelphia, PA 19104

There is often overlap in the diagnostic features of common pathologic processes such as infection, sterile inflammation, and cancer both clinically and using conventional imaging techniques. Here, we report the development of a positron emission tomography probe for live bacterial infection based on the small-molecule antibiotic trimethoprim (TMP). [18F]fluoropropyl-trimethoprim, or [18F]FPTMP, shows a greater than 100-fold increased uptake in vitro in live bacteria (*Staphylococcus aureus*, *Escherichia coli*, and *Pseudomonas aeruginosa*) relative to controls. In a rodent myositis model, [18F]FPTMP identified live bacterial infection without demonstrating confounding increased signal in the same animal from other etiologies including chemical inflammation (turpentine) and cancer (breast carcinoma). Additionally, the biodistribution of [18F]FPTMP in a nonhuman primate shows low background in many important tissues that may be sites of infection such as the lungs and soft tissues. These results suggest that [18F]FPTMP could be a broadly useful agent for the sensitive and specific imaging of bacterial infection with strong translational potential.

bacteria | imaging | PET | trimethoprim | radiotracer

The distinction between bacterial infection and other disease entities such as sterile inflammation and cancer can be challenging on the basis of symptoms and physical findings. In addition, it is accepted that there can be significant overlap between bacterial infection, inflammation, and cancer using both standard diagnostic imaging techniques [e.g., computed tomography, contrast-enhanced magnetic resonance imaging, and positron emission tomography (PET)] and laboratory studies (e.g., white blood cell count, erythrocyte sedimentation rate) (1, 2). This lack of diagnostic feature specificity is especially conspicuous when the pretest probability of the least likely etiology is higher due to individual variability such as genetic predisposition or known malignant disease and/or when perturbations such as prior surgery or radiotherapy alter the normal anatomy and provoke an inflammatory tissue reaction. Thus, the resulting final diagnostic interpretation cannot differentiate among the possibilities including cancer, infection, or inflammation, an unsettling outcome for patient and clinician alike.

Other important implications of a bacterial-specific imaging agent could include decreasing inappropriate use of antibiotics, which are often given empirically; the avoidance of invasive procedures such as a biopsy with potential for complications; and the ability to monitor bacterial burden after initiation of antibiotic treatment, for example, in the case of orthopedic hardware infection. Given these clear potential uses, past efforts have focused largely on nuclear techniques based on radiotracers derived from peptides, antibiotics, and sugars due to the required sensitivity needed for identifying bacteria (3, 4). Still, no bacterial imaging agent is routinely used clinically, and among the previously developed agents many are not sufficiently broad spectrum to provide strong negative and positive predictive values to inform clinical decision making. Older techniques such as labeled white blood cell and gallium scanning and emerging fluorodeoxy-glucose (FDG) PET do not bind the bacteria themselves and thus do not give a quantitative measure of the bacterial burden, and some of these techniques have suboptimal protocols including two-step processes or next-day imaging for routine clinical practice (4, 5).

To address this clinical challenge, we sought to make a small-molecule PET probe to identify bacterial infection in vivo, which would not be confounded by chemical inflammation or cancer (Fig. 1A). The probe is based on the synthetic antibiotic trimethoprim (TMP) that inhibits bacterial dihydrofolate reductase (dhfr), an enzyme in the DNA synthesis and folate pathway that is conserved across most bacterial species including both Gram-positive, Gram-negative, mycobacterial species such as *Mycobacterium tuberculosis* and some parasites such as *Toxoplasma gondii* (*SI Appendix*, Fig. S1) (6, 7). TMP has nanomolar affinity for dhfr whereas it has micromolar affinity for human dihydrofolate reductase (DHFR) and is known to be amenable to synthetic modifications without loss of affinity (8–10). Thus, we developed a TMP-based radiotracer, [18F]fluoropropyl-trimethoprim, or [18F]FPTMP, tested its uptake in mammalian and bacterial cells in vitro, and tested in vivo its ability to identify common pathogenic bacteria such as *Staphylococcus aureus*, *Escherichia coli*, as well as *Pseudomonas aeruginosa*, which uses an efflux pump as a mechanism of antibiotic resistance (11). Additionally, we tested [18F]FPTMP in a nonhuman primate to shed light on the expected human tissue biodistribution if this radiotracer were to be used for noninvasive diagnosis of bacterial infections in patients.

Results

[18F]FPTMP was synthesized via a five-step reaction to make the mesylate precursor for radiofluorination (Fig. 1B; see *SI Appendix, Materials and Methods* for detailed synthetic procedures). Prior structure–activity relationships of trimethoprim have shown that the paramethoxy position was amenable to synthetic

Significance

The ability to distinguish bacterial infection from other pathologies in humans can be challenging. An imaging agent with great sensitivity and spatial resolution that would allow noninvasive identification of sites of bacterial infection could increase our understanding of the natural history of bacterial infection in patients and potentially be used to support clinical decision making. Here, we report the first synthesis of a fluorine-18–labeled derivative of the antibiotic trimethoprim for positron emission tomography imaging and show that it can identify bacterial infection in rodents. Importantly, this radiotracer does not accumulate at sites of sterile inflammation or cancer, pathologies that often have overlapping imaging features with bacterial infection.
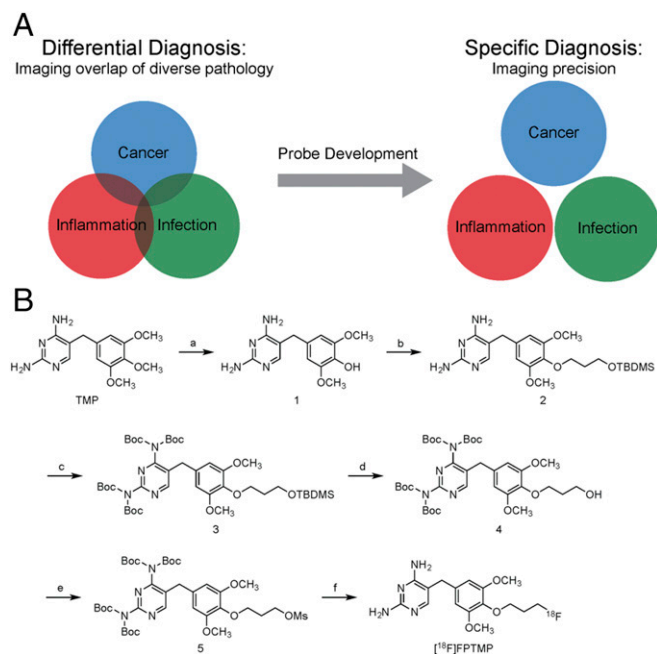
Fig. 1. Probe development for separating overlapping pathologies. (*A*) Pathologies such as infection, inflammation, and cancer often have overlapping conventional imaging features. Distinction between such basic underlying pathologies with probe development can be important for accurate diagnosis or monitoring of therapy, such as in the case of bacterial infection. (*B*) Synthetic scheme for [18F]-radiolabeled trimethoprim, [18F]FPTMP, for imaging bacterial infection.

modifications including adaptation of fluorescent conjugates or heterodimer-related moieties (10, 12). Briefly, TMP was converted to the phenol, the propyl-silyl-ether protecting group was added at the paraposition, the aromatic heterocyclic amine groups were bis-boc protected, and the propyl-mesylate was made. Radiofluorination was performed with Kryptofix with good radiosynthetic yield, 99% radiochemical purity, and high specific activity (between 5,000 and 15,000 Ci/mmol).

Human HCT116 cells were engineered to express *E. coli* dhfr as previously described (13) and used to test whether the affinity of [18F]FPTMP was similar to reported values of TMP for dhfr. It was not expected that TMP would have any activity in mammalian cells as the I_{50} (concentration that inhibits 50% of DHFR activity) of TMP for human DHFR is 490,000 nM, whereas the I_{50} for *E. coli* dhfr is 7 nM (14). Additionally, radiotracer concentrations are usually in the picomolar concentration range. The B_{max} in HCT116 dhfr cells was $2,870 \pm 106$ fmol/mg and the K_D was 0.465 nM (*SI Appendix*, Fig. S2), noting the dissociation constant of parent TMP for dhfr was reported as 7–15 nM in recombinant protein studies (14).

Each bacterial species was tested for sensitivity to TMP and unlabeled FPTMP (Fig. 2*A*). Unlabeled FPTMP was synthesized as described in *SI Appendix*, Scheme 1. There was no difference in the minimum inhibitory concentration (MIC) of *Staphylococcus aureus* (4 mg/L), a small difference in *E. coli* (4–8 mg/L), and, as expected, *P. aeruginosa* was resistant to TMP and FPTMP. These values closely align with literature-reported sensitivity values (15).

Cell uptake experiments with [18F]FPTMP in live bacteria showed strong signal increases in comparison to competition with excess unlabeled compound (Fig. 2 *B*–*D*). *S. aureus* and *P. aeruginosa* showed an almost 100-fold increased signal at 3 h and *E. coli* an almost 1,000-fold increased signal (Fig. 2*D*). Additionally, there was rapid uptake, within 15 min in Gram-positive *S. aureus* and Gram-negative *E. coli*. *P. aeruginosa* required a longer time to reach saturation, ~2 h, and an overall lower level of uptake compared with

the other bacterial species per cfu (Fig. 2*B*). Competition experiments were performed with a total of 3 h of incubation for each bacteria with [18F]FPTMP and addition of excess unlabeled TMP at various time points before assessment. Both *S. aureus* and *P. aeruginosa* demonstrate rapid return to background uptake levels, even after only 15 min of incubation with excess unlabeled TMP (Fig. 2*C*). Competition with excess unlabeled TMP in *E. coli* reaches equilibrium more slowly, returning to background levels at 60 min.

Additional studies showing uptake of live versus heat-killed bacteria also demonstrated convincing specificity of uptake, with minimal uptake in the heat-killed bacteria over varied levels of cfu and with *S. aureus* in addition to *E. coli* (*SI Appendix*, Figs. S3 and S4).

In vivo biodistribution of [18F]FPTMP in BALB/c mice at 15, 60, and 120 min revealed strong initial uptake in the kidneys and delayed uptake in the liver and gallbladder (Fig. 3*A*). Many tissues that are frequent sites of clinical infections, including the blood/heart, muscle, lung, skin, and brain, have very low retention by 60–120 min: <0.3% percentage of injected dose (ID/g) (Fig. 3*B*). Tissues that have increased background include intestines/stool, with a modest amount of uptake in bone, which includes marrow (2.03% ID/g), and thyroid (2.39% ID/g). We tested the uptake in bone marrow compared with cortical bone and found that there are components of [18F]FPTMP binding to
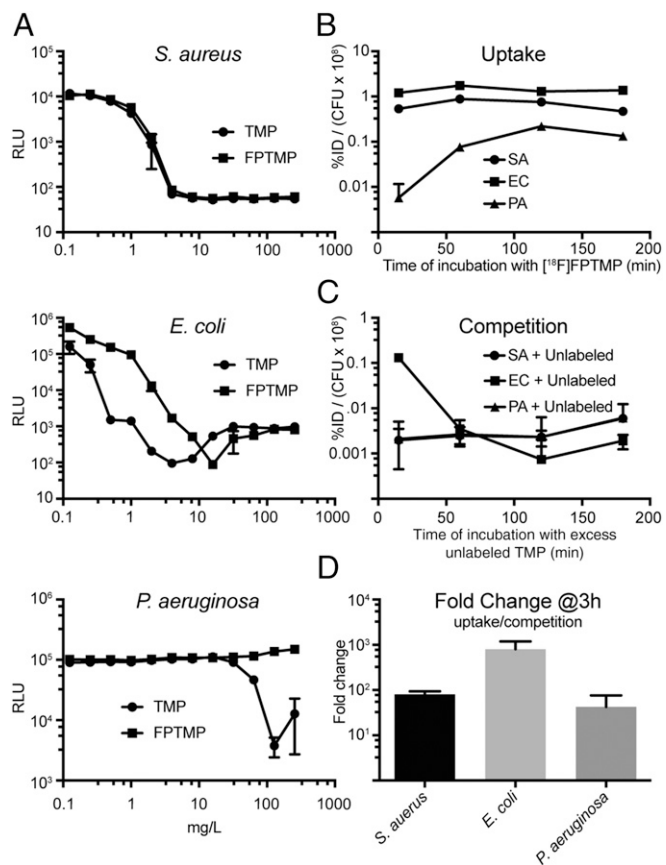

Fig. 2. MIC calculation with unlabeled FPTMP and in vitro uptake of [18F]FPTMP with different species of bacteria. (*A*) A MIC experiment was performed by varying concentrations of TMP and FPTMP with *S. aureus*, *E. coli*, and *P. aeruginosa*. Incubation occurred overnight at 37 °C, and luminescence (relative luminescence units, RLU) assessment was performed the next day. (*B* and *C*) Time course of uptake and competition in the bacterial cultures at 37 °C in terms of percentage of injected dose (%ID) per colony forming units (cfu × 10^8). Error bars represent the SD (*n* = 3). (*D*) Fold change of uptake in cultures of *S. aureus*, *E. coli*, and *P. aeruginosa* after a 3-h incubation with and without excess unlabeled (cold) TMP (10 μM). SA, *S. aureus*; EC, *E. coli*; PA, *P. aeruginosa*.

both tissues (*SI Appendix*, Fig. S5). In anticipation of human imaging, OLINDA/EXM 1.1 was used to estimate human dosimetry in an adult female with an estimated effective dose 0.43 mSv from a 10-mCi (standard 370 MBq) injection of [^{18}F]FPTMP (*SI Appendix*, Fig. S6) (16).

Given promising in vitro experimental results, a rodent myositis model was chosen for in vivo testing. All three species of bacteria (*S. aureus*, *E. coli*, and *P. aeruginosa*) were auto-bioluminescent and carried the lux operon, which provided an optical readout of infection locale and extent. *E. coli* was used for our initial testing of the sensitivity of detection, i.e., the fewest number of bacteria detectable with [^{18}F]FPTMP in vivo. Live *E. coli* were injected 1 d before imaging in the hindlimb, forelimb, and ear pinna at $1 \times E8$, $1 \times E7$, and $1 \times E6$ cfu, respectively, with an equal number of heat-killed bacteria injected contralaterally. Bioluminescence imaging confirmed relative concentrations of bacteria and bacterial location (Fig. 4 *A* and *B*). After [^{18}F]FPTMP injection, there was a nearly threefold increased uptake in live *E. coli* in the right hindlimb compared with the area of heat-killed bacteria as measured by normalizing the signal to injected dose and animal weight (Fig. 4 *C* and *D*). The retention of signal in live bacteria was evident by 40 min after injection and achieved maximal target to background signal at 90 min (Fig. 4*E*). As expected from the biodistribution study, there was uptake from nearby bone/bone marrow. Confirming uptake from the expected sites of myositis, autoradiography of two animals showed diffuse uptake from the muscle of the hindlimb of the infected animal (Fig. 4*F*). Bacterial infection was not consistently detectable in the forelimb or ear pinna by PET imaging or by autoradiography. Microscopy of Gram-stained sections showed *E. coli* infection among the muscle fibers of the hindlimb (Fig. 4*G*).

A critical experiment was whether [^{18}F]FPTMP could provide imaging specificity among three potentially overlapping diagnoses: infection, inflammation, and cancer. To test [^{18}F]FPTMP specificity for bacterial infection, we designed an experiment in which each these processes were implanted in a different part of the mouse (Fig. 5*A*). The 4T1(Luc+) mouse mammary carcinoma cells were injected in the left shoulder region, turpentine (30 µL) was injected in the left hindlimb, and, again, live *E. coli* ($1 \times E8$ cfu) in the right hindlimb. Turpentine was injected 2 d before [^{18}F]FPTMP imaging, and *E. coli* and tumor cells were injected the night before [^{18}F]FPTMP imaging with [^{18}F]FDG imaging completed the next day. The presence of tumor cells was confirmed by bioluminescence imaging, and the presence of inflammation related to turpentine injection was confirmed by histology (*SI Appendix*, Fig. S7). As shown by imaging, there was no significant [^{18}F]FPTMP accumulation in sterile/chemical inflammation with turpentine or in the 4T1 tumors, whereas there was focal, increased uptake in the
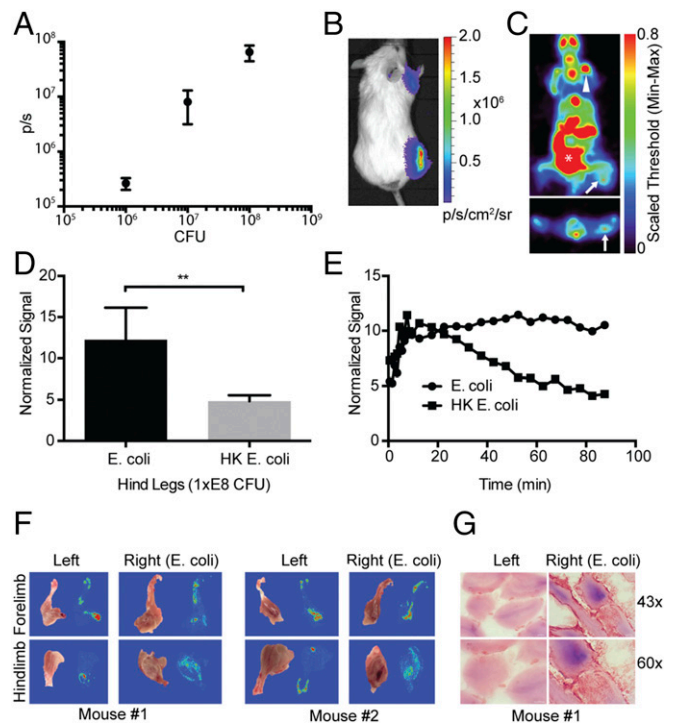

Fig. 4. Limits of detectability of *E. coli* infection in vivo. (*A*) Live bioluminescent *E. coli* were injected intramuscularly (i.m.) into the right hindlimb ($1 \times E8$ cfu), right forelimb ($1 \times E7$), and ear pinna ($1 \times E6$) of BALB/c mice, whereas heat-killed (HK, 95 °C for 20 min) *E. coli* were injected into the contralateral limb. The graph shows colony-forming units (*x* axis, cfu) versus bioluminescent light flux (p/s). Error bars represent the SD ($n = 3$). (*B*) Representative bioluminescent image of data from *A*. (*C*) Transverse and coronal images of a representative mouse after [^{18}F]FPTMP, ∼200 µCi i.v. at 90 min. Live bacteria (arrow), bone (arrowhead), and bowel (*) are identified. (*D*) Normalized signal from the hindlimb (lower leg, $n = 3$). $P < 0.01$ using a two-tailed student's *t*-test. (*E*) Time-activity curve of uptake from the hindlimbs of a representative animal. (*F*) Autoradiography after in vivo administration of [^{18}F]FPTMP of two animals from *C*. Diffuse uptake was seen in the musculature of the lower legs infected with live *E. coli*. (*G*) Bright-field microscopy of tissue gram stains of the infected and control lower legs at 40× and 63×. *E. coli* is a Gram-negative rod and stains a red/pink color.

infected muscle (Fig. 5 *B* and *C*). Quantitatively, there was nearly a 300% increase in [^{18}F]FPTMP in the infection-to-muscle ratio (target-to-muscle ratio of 2.7), whereas there was little to no increased uptake in inflammation (target-to-muscle ratio of 1.0) or tumor-to-muscle ratio (target-to-muscle ratio of 1.3, Fig. 5*D*), noting previous evidence of a lack of tumor TMP uptake (13). Conversely, a standard PET radiotracer, [^{18}F]FDG, showed increased uptake in all etiologies, infection, inflammation, and cancer.

In addition to *E. coli*, [^{18}F]FPTMP consistently detected *S. aureus* ($1 \times E8$ cfu) in the myositis model (*SI Appendix*, Figs. S8 and S9), noting that many strains of *S. aureus* are sensitive to the antibiotic combination trimethoprim–sulfamethoxazole. *P. aeruginosa*, however, was not detectable in vivo (*SI Appendix*, Fig. S10). Two contributing factors to this finding could be that *P. aeruginosa* was injected at a lower injected dose ($1 \times E7$ cfu) due toxicity at higher doses and the overall lower uptake in *P. aeruginosa* as evidenced in vitro (Fig. 2).

Finally, because rodents have different levels of circulating folate pathway metabolites, different metabolic rates, and different pharmacokinetics from primates, we tested [^{18}F]FPTMP in a nonhuman primate, the rhesus monkey. Monkeys were injected with 1–2 mCi of [^{18}F]FPTMP i.v. and imaged over 1.5–2 h. Imaging time-activity curves were generated from tissues of interest
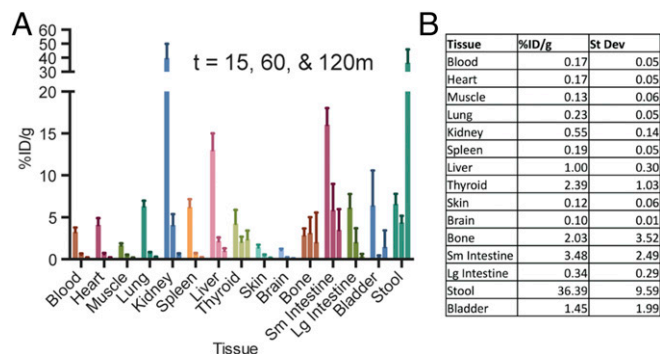

Fig. 3. Rodent biodistribution of [^{18}F]FPTMP. (*A*) Tissue biodistribution of [^{18}F]FPTMP, ∼100 µCi i.v., at 15, 60, and 120 min. Bars for each tissue type represent those respective time points moving left to right. (*B*) Table of uptake in %ID/g at 120 min from assayed tissues.

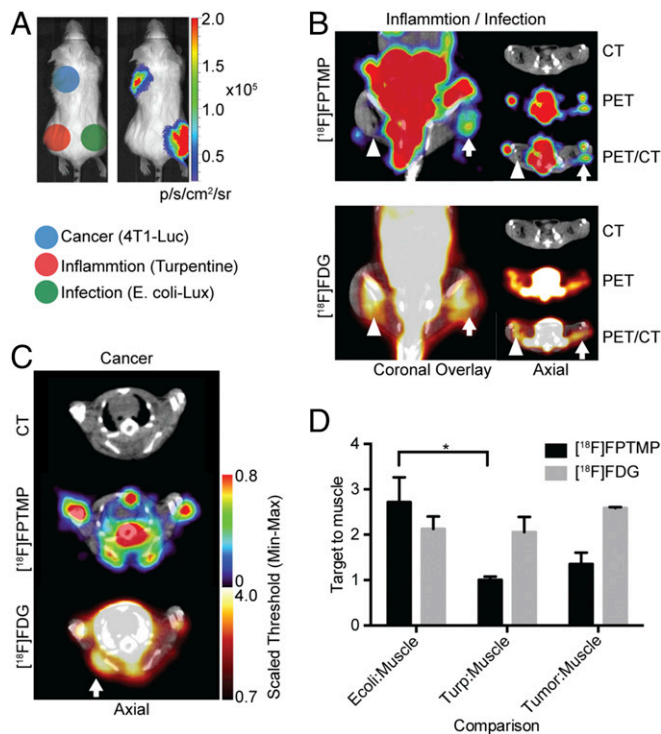| Tissue	%ID/g	St Dev
Blood	0.17	0.05
Heart	0.17	0.05
Muscle	0.13	0.06
Lung	0.23	0.05
Kidney	0.55	0.14
Spleen	0.19	0.05
Liver	1.00	0.30
Thyroid	2.39	1.03
Skin	0.12	0.06
Brain	0.10	0.01
Bone	2.03	3.52
Sm Intestine	3.48	2.49
Lg Intestine	0.34	0.29
Stool	36.39	9.59
Bladder	1.45	1.99

Fig. 5. [^{18}F]FPTMP detects live bacterial infection, not cancer or inflammation. (*A*) Schematic of locations of infection, inflammation, and cancer in a BALB/c mouse. Mouse mammary carcinoma cells (4T1Luc+, 1 million) were injected s.c. over the left shoulder of the mouse. Chemical inflammation with turpentine (30 μL IM) was induced 2 d before [^{18}F]FPTMP imaging and 3 d before FDG imaging. Live *E. coli* bacteria (1 × E8 cfu i.m.) were injected into the right lower leg. (*Right*) Bioluminescent imaging of a representative animal after D-luciferin injection (1 mg, i.p.) illustrating active bacterial infection in the right leg and live tumor cells in the left shoulder region. (*B*) A representative animal after [^{18}F]FPTMP, ~200 μCi i.v., shows uptake in the infected hindlimb muscle (arrow) 4 h after infection, but not in the area of turpentine injection (arrowhead). Next-day imaging with [^{18}F]FDG, ~300 μCi i.v., shows uptake in both infection and chemical inflammation 1 h after injection. (*C*) The same animal as in *B* is shown after [^{18}F]FPTMP and [^{18}F]FDG injection at the site of a 4T1 tumor. There is increased [^{18}F]FDG uptake at the site of the tumor and no specific signal from [^{18}F]FPTMP. (*D*) Quantification of the data from *B* and *C*. Error bars represent the SD (n = 4). *P < 0.05.

(Fig. 6 *A–C*), and a 3D rendering of monkey 1 showed low tracer background in many tissues of interest (Fig. 6*D*). Peripheral bone uptake was much less conspicuous than in the mouse models, for example, in long bones including the humerus (Fig. 6 *C* and *D*). The dominant signal from the animal was the gallbladder, related to hepatobiliary excretion of the tracer, and notably there was increasing signal over time in the thoracic spine (Fig. 6*C*).

Discussion

Imaging is uniquely suited to be a conduit between accurate diagnosis and monitoring response to precision therapy, important components of the precision medicine initiative (17, 18). We built on past efforts to develop an imaging tool that specifically identifies live bacteria without confounding signal from sterile inflammation or cancer. Bacteria, from a different phylogenetic domain, should have molecular imaging targets more diverse and accessible for imaging pathology than, for example, a cancer cell, where there are just a few genetic mutations to differentiate that cancer cell from normal host tissues (4). With this in mind, we revisited the idea of an antibiotic PET radiotracer because of the small-molecule characteristics of the antibiotic and the sensitivity and spatial localization of PET.
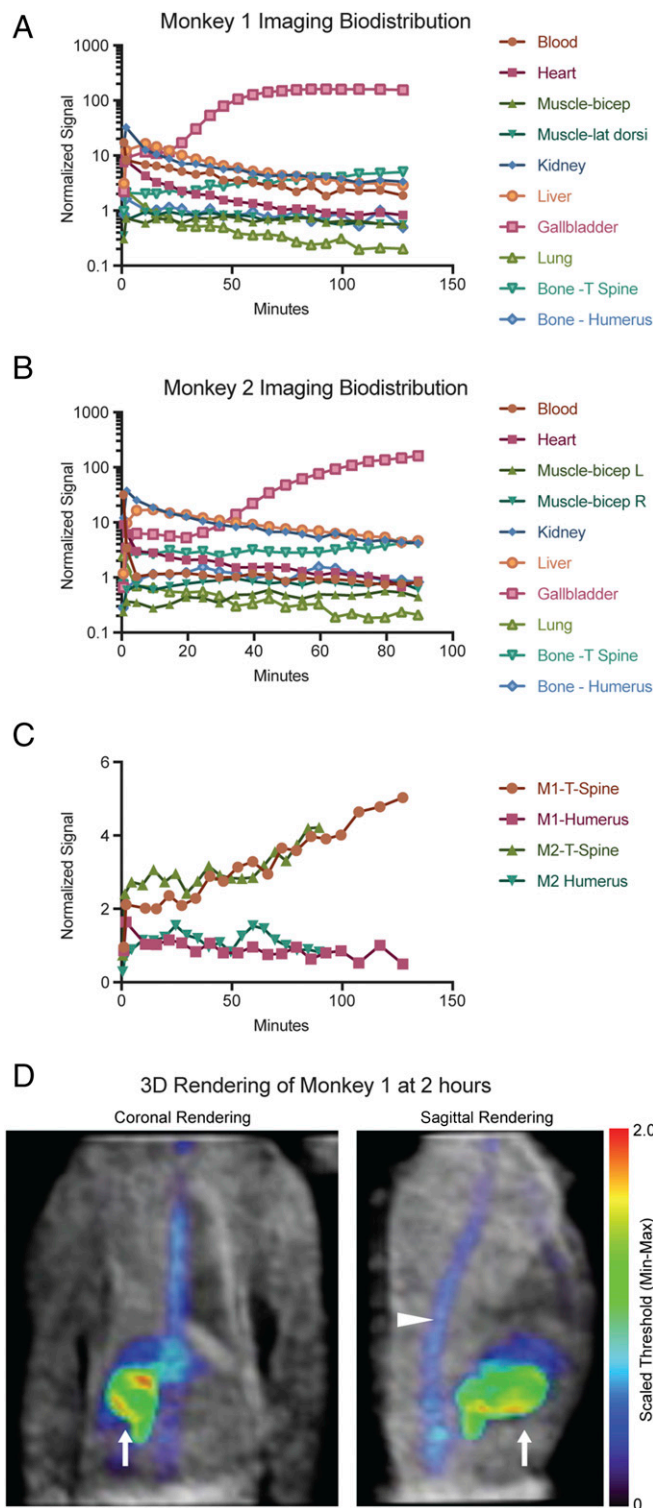
Fig. 6. Imaging biodistribution in nonhuman primates. (*A* and *B*) Two rhesus monkeys were injected with [^{18}F]FPTMP 1–2 mCi i.v. and a graphical imaging biodistribution over time is shown. Regions of interest within tissues were quantified and normalized to injected weight and dose. (*C*) Focused graph of normalized signal over time in the spine and humerus of both monkeys. (*D*) The grayscale image represents the transmission data of monkey 1, and the NIH color scale represents [^{18}F]FPTMP at 2 h. Images of the thorax and upper abdomen of the animal are presented in the coronal and sagittal plane. Signal is seen predominantly from the gallbladder (arrow) with a small component from the spine (arrowhead).

It is surprising, perhaps, that this advancement comes at a time when interest in antibiotic radiotracers for imaging infection has waned, especially after tracer derivatives of ciprofloxacin have had mixed clinical results (4, 19). Further in vitro studies with quinolone radiotracers showed binding to heat-killed bacteria and nonspecific uptake in the presence of excess unlabeled compound, tempering enthusiasm for clinical use (20, 21). Other groups have investigated metabolic agents such as fialuridine (FIAU) and radiolabeled sugars such as sorbitol and maltose. A clinical trial with [^{124}I]FIAU was recently stopped due to nonspecific uptake in the adjacent muscle and difficulty identifying orthopedic prosthetics with active infection (22). Radiolabeled sugars, although showing promise in small animal experiments and with select bacterial species, generally do not carry the same broad-spectrum bacterial affinity that TMP does or the sugar has a relatively high background uptake in normal tissues; for example, 6-[^{18}F]-fluoromaltose has blood pool and lung uptake of >4% ID/g at 2 h compared with that of [^{18}F]FPTMP, ~0.2% ID/g at 2 h (Fig. 3B) (3, 23). Thus, the positive and negative predicative values using these tracers is less likely to be robust, a crucial component for clinical decision making. Moreover, currently used nuclear techniques such as white blood cell and gallium scanning, both of which are used sparingly, have protocol-related limitations and can have confounding uptake from noninfectious inflammation (4). These and other innovative investigations highlight the need for bacterial imaging agents that move the infection diagnostics beyond laboratory values, biopsy, and cultures.

We chose TMP as a PET probe because of several attractive features of the small molecule. The characteristics of absorption, distribution, metabolism, and excretion are favorable with a relatively short blood half-life in humans, low serum protein binding (~50%), and broad tissue distribution (24, 25). Additionally, TMP is a well-studied chemical biology tool, is tolerant of large adorning chemical modifications, and is a well-known, clinically used antibiotic with antimicrobial activity against Gram-positive, Gram-negative, and some mycobacterial and parasitic species (10). In combination, these features suggested that TMP would satisfy many of the requirements of a good imaging agent and be worthy of investigation.

TMP has nanomolar affinity for its bacterial protein target, dhfr, and we synthesized the [^{18}F]fluoropropyl derivative, [^{18}F]FPTMP. The [^{18}F]fluorethyl derivative was attempted first, but produced several side products potentially related to decreased rotational freedom and increased proximity of the fluorine to the TMP heterocycle. As expected from prior structure–activity relationship (SAR) studies of TMP (10), the [^{18}F]fluoropropyl derivative had little affect on the binding constant for E. coli dhfr (0.46 nM) in transgenic mammalian cells. We chose testing the binding constant in mammalian cells given that we could express the canonical protein target of TMP, E. coli dhfr, and given that these cells are adherent, which facilitates procedural wash steps. We expect that other isotopes and even chelators may be adapted to this para-methoxy position of trimethoprim; however, as dhfr is an intracellular protein, diffusion/transport across the cell membrane or wall may be problematic with larger modifications.

Unlabeled FPTMP had similar MIC values to TMP, suggesting the ability to cross the bacterial cell membrane. As expected, P. aeruginosa shows resistance to TMP and FPTMP (Fig. 2A).

[^{18}F]FPTMP shows rapid uptake in vitro in three different bacterial species, with ~100–1,000-fold increases in signal above background. This magnitude of signal induction in vitro is probably necessary for such a radiotracer to provide discernible bacterial signal in living animals where the physical size of bacteria and the target protein concentration can be dwarfed by adjacent tissues and nonspecific binding (26). One limitation of using TMP as a bacterial imaging agent is that mechanisms of antibiotic resistance used by bacteria could affect the uptake. This is illustrated in part by the uptake of P. aeruginosa that shows delayed and decreased overall uptake at saturation in vitro (Fig. 2B). The prime mechanism of P. aeruginosa resistance to TMP is due to

small-molecule export pump (11, 27). Small-molecule efflux is most consistent with a lower overall level of uptake at saturation; however, we cannot exclude that an altered K_i for Pseudomonas dhfr is also involved and could contribute to the delayed uptake. Note that detailed evaluation of the affinity of trimethoprim for different bacterial dhfr proteins has been previously performed (14).

Other trimethoprim resistance mechanisms include dhfr overexpression (E. coli), which would actually increase [^{18}F]FPTMP uptake or a mutant binding site that would decrease uptake. Binding site mutations are sometimes present in the bacterial genome via duplicated copies of the dhfr gene (plasmid/integron); thus the native dhfr may still be present for uptake/targeting (28). Clearly, any targeted molecular imaging agent may suffer variability based on the expression of the target in the pathologic process of interest; however, the strong in vitro uptake of [^{18}F]FPTMP in these three common Gram-positive and Gram-negative bacterial pathogens bodes well.

In the animal biodistribution of [^{18}F]FPTMP, the bone uptake appears to be less of an issue in primates, where there was low uptake in the humerus, for example (Fig. 6C). The difference between mouse and primate bone uptake could be related to the known phenomenon of increased defluorination in rodents (29) and suggests that [^{18}F]FPTMP may still be considered for human osteomyelitis imaging, especially in the periphery. Interestingly, there was continued, slow accumulation in the monkey thoracic spine (Fig. 6C). This suggests that there is increased binding in hematopoietic cells rather than in cortical bone that would be related to uptake from [^{18}F] defluorination. Supporting these conclusions are the facts that (i) the autoradiography signal colocalizes with red marrow (Fig. 4F), (ii) hematopoietic bone marrow has relatively high levels of mammalian DHFR and is a site of methotrexate toxicity (a high-affinity mammalian DHFR inhibitor) (30), and (iii) a limited biodistribution experiment in mice shows increased uptake in cortical bone as well as red marrow (SI Appendix, Fig. S5)—all of which indicate that the bone marrow may have some slow, low level of [^{18}F]FPTMP accumulation. As expected, identifying infection in the abdominal and pelvic compartments may be limited given mixed hepatobiliary and renal excretion of the tracer. For example, if an abdominal abscess were adjacent to the bowel, it would be difficult to definitively separate these entities and identify the infection. Reassuringly, in mouse and monkey, there was low background in many tissues of interest including blood/heart, lung, brain, muscle, and soft tissues.

In a mouse myositis model, [^{18}F]FPTMP identified sites of bacterial infection with E. coli and S. aureus (1 × E8, Fig. 4 and SI Appendix, Fig. S9). The threshold of detection compared with background in E. coli in mice appears to be 1 × E8 cfu, noting that lower injected bacterial doses in the forelimb and ear pinna were not detectable by PET imaging or autoradiography above background. The overall increased uptake in infected limbs compared with control was two- to threefold depending on the experiment. In their seminal [^{18}F]fluorodeoxysorbitol (FDS) paper, Weinstein et al. used heat-killed bacteria as a control rather than turpentine (similar to Fig. 4), which showed an impressive approximately sevenfold increased uptake in the infected muscle, again noting the caveat that FDS is best used for a subset of bacterial species, specifically Enterobacter and several other Gram-negative bacteria, and not for common pathogens such as Staphylococcus, Streptococcus, and Enterococcus (3). ^{18}F-fluoromaltose appears to have an approximately twofold increased uptake in infected tissues relative to controls (23).

P. aeruginosa infection required a lower bacterial load (1 × E7 cfu) given observed toxicity at higher bacterial burden and was not detectable above background with [^{18}F]FPTMP (SI Appendix, Fig. S10). This is consistent with the lower uptake in vitro and a known drug export pump in P. aeruginosa. Although small animal imaging is more limited, the 100-fold increase in P. aeruginosa uptake in vitro warrants further investigation to determine whether P. aeruginosa would be detectable in larger animals and humans.

Importantly, [^{18}F]FPTMP achieved the goal of imaging bacterial infection in vivo without any confounding uptake in sterile/chemical inflammation or mouse breast carcinoma. There was a nearly 300% increase in [^{18}F]FPTMP uptake in live *E. coli* infection compared with turpentine, which is notable considering that clinicians use 30% increases or decreases in PET signal to make management decisions for cancer patients, for example (31). In contrast, [^{18}F]FDG had increased uptake in all three pathologies.

Limitations of the study include the difficulty of determining how well these results would translate to human clinical situations. For example, it is hard to determine if the [^{18}F]FPTMP target-to-background ratios would correlate in the setting of human hardware infection, given the local metal artifact and potentially low numbers of bacteria that may be present in a biofilm or otherwise. Future directions include testing [^{18}F]FPTMP in more bacterial species and infection models (e.g., pneumonia) and testing in larger animals such as rats that, given their larger size, may allow better detection of lower injected doses of bacteria. Additional upcoming studies include monitoring antibiotic therapy in animal models, extending preclinical evaluation to mycobacteria and parasites, and initiating human clinical trials.

A new PET radiotracer, [^{18}F]FPTMP, can specifically image live bacteria in rodent models and does not accumulate at sites of inflammation or tumor. Primate biodistribution appears favorable for human imaging and upcoming clinical trials with [^{18}F]FPTMP will help determine whether this radiotracer can identify live bacterial infection in patients and can support clinical decision making.

Materials and Methods

Please see *SI Appendix, Materials and Methods*, for complete materials and methods including [^{18}F]FPTMP and FPTMP synthesis, mammalian and bacterial cell culture, and in vitro and in vivo assays. Briefly, adherent transgenic HCT116 mammalian cells expressing *E. coli* dhfr were used to test the in vitro uptake and K_D of [^{18}F]FPTMP. *S. aureus* (8325-4; P2) lux::Cm (chloramphenicol resistant), *E. coli* (GR12) EM7-lux::K_m [kanamycin resistant, made in similar manner to Lane et al. (32)], and *Pseudomonas aeruginosa* Xen5 (American Type Culture Collection 19660) lux::Tc (tetracycline resistant) were gifts of the Chris Contag laboratory, Stanford University, Stanford, CA. All bacteria were auto-bioluminescent and bioluminescence is not known to affect pathogenicity or drug uptake (33). A mouse model of myositis was used to confirm uptake in infected tissues and not in tissues with sterile inflammation or cancer. Rhesus monkeys were given a bolus injection of the radiotracer (~1–2 mCi) followed by a saline flush with the concurrent start of dynamic list mode data acquisition for 1.5–2 h (*n* = 2). Imaging was performed with two different monkeys. All mouse and monkey studies were performed in accordance with approval from the Institutional Animal Care and Use Committee (University of Pennsylvania).

1. Heuker M, et al. (2016) Preclinical studies and prospective clinical applications for bacteria-targeted imaging: The future is bright. *Clin Transl Imaging* 4:253–264.
2. Palestro CJ, Love C, Miller TT (2007) Diagnostic imaging tests and microbial infections. *Cell Microbiol* 9:2323–2333.
3. Weinstein EA, et al. (2014) Imaging Enterobacteriaceae infection in vivo with 18F-fluorodeoxysorbitol positron emission tomography. *Sci Transl Med* 6:259ra146.
4. Palestro CJ (2009) Radionuclide imaging of infection: In search of the grail. *J Nucl Med* 50:671–673.
5. van Oosten M, et al. (2015) Targeted imaging of bacterial infections: Advances, hurdles and hopes. *FEMS Microbiol Rev* 39:892–916.
6. Forgacs P, et al. (2009) Tuberculosis and trimethoprim-sulfamethoxazole. *Antimicrob Agents Chemother* 53:4789–4793.
7. Torre D, et al.; Italian Collaborative Study Group (1998) Randomized trial of trimethoprim-sulfamethoxazole versus pyrimethamine-sulfadiazine for therapy of toxoplasmic encephalitis in patients with AIDS. *Antimicrob Agents Chemother* 42:1346–1349.
8. Baccanari DP, Daluge S, King RW (1982) Inhibition of dihydrofolate reductase: Effect of reduced nicotinamide adenine dinucleotide phosphate on the selectivity and affinity of diaminobenzylpyrimidines. *Biochemistry* 21:5068–5075.
9. Chan DC, Fu H, Forsch RA, Queener SF, Rosowsky A (2005) Design, synthesis, and antifolate activity of new analogues of piritrexim and other diaminopyrimidine dihydrofolate reductase inhibitors with omega-carboxyalkoxy or omega-carboxy-1-alkynyl substitution in the side chain. *J Med Chem* 48:4420–4431.
10. Calloway NT, et al. (2007) Optimized fluorescent trimethoprim derivatives for in vivo protein labeling. *Chembiochem* 8:767–774.
11. Huebinger RM, et al. (2016) Targeting bacterial adherence inhibits multidrug-resistant Pseudomonas aeruginosa infection following burn injury. *Sci Rep* 6:39341.
12. De Clercq DJ, Tavernier J, Lievens S, Van Calenbergh S (2016) Chemical dimerizers in three-hybrid systems for small molecule-target protein profiling. *ACS Chem Biol* 11:2075–2090.
13. Sellmyer MA, et al. (2017) Quantitative PET reporter gene imaging with [(11)C]trimethoprim. *Mol Ther* 25:120–126.
14. Baccanari DP, Kuyper LF (1993) Basis of selectivity of antibacterial diaminopyrimidines. *J Chemother* 5:393–399.
15. European Committee for Antimicrobial Susceptibility Testing of the European Society of Clinical Microbiology and Infectious Diseases (2003) Determination of minimum inhibitory concentrations (MICs) of antibacterial agents by broth dilution. *Clin Microbiol Infect* 9:1–7.
16. Stabin MG, Sparks RB, Crowe E (2005) OLINDA/EXM: The second-generation personal computer software for internal dose assessment in nuclear medicine. *J Nucl Med* 46:1023–1027.
17. Weissleder R, Schwaiger MC, Gambhir SS, Hricak H (2016) Imaging approaches to optimize molecular therapies. *Sci Transl Med* 8:355ps16.
18. Collins FS, Varmus H (2015) A new initiative on precision medicine. *N Engl J Med* 372:793–795.
19. Benitez A, Roca M, Martin-Comin J (2006) Labeling of antibiotics for infection diagnosis. *QJ Nucl Med Mol Imaging* 50:147–52.
20. Siaens RH, Rennen HJ, Boerman OC, Dierckx R, Slegers G (2004) Synthesis and comparison of 99mTc-enrofloxacin and 99mTc-ciprofloxacin. *J Nucl Med* 45:2088–2094.
21. Sarda L, et al. (2003) Inability of 99mTc-ciprofloxacin scintigraphy to discriminate between septic and sterile osteoarticular diseases. *J Nucl Med* 44:920–926.
22. Zhang XM, et al. (2016) [(124)I]FIAU: Human dosimetry and infection imaging in patients with suspected prosthetic joint infection. *Nucl Med Biol* 43:273–279.
23. Gowrishankar G, et al. (2014) Investigation of 6-[^{18}F]-fluoromaltose as a novel PET tracer for imaging bacterial infection. *PLoS One* 9:e107951.
24. Kremers P, Duvivier J, Heusghem C (1974) Pharmacokinetic studies of co-trimoxazole in man after single and repeated doses. *J Clin Pharmacol* 14:112–117.
25. Ingebrigtsen K, Skoglund LA, Nafstad I (1990) A study on melanin affinity of 14C-trimethoprim in male Mol:WIST and Mol:PVG rats. *Zeitschrift fur Versuchstierkunde* 33:73–77.
26. Cheng G, Werner TJ, Newberg A, Alavi A (2016) Failed PET application attempts in the past: Can we avoid them in the future? *Mol Imaging Biol* 18:797–802.
27. Maseda H, Yoneyama H, Nakae T (2000) Assignment of the substrate-selective subunits of the MexEF-OprN multidrug efflux pump of *Pseudomonas aeruginosa*. *Antimicrob Agents Chemother* 44:658–664.
28. Eliopoulos GM, Huovinen P (2001) Resistance to trimethoprim-sulfamethoxazole. *Clin Infect Dis* 32:1608–14.
29. Ponde DE, et al. (2007) 18F-fluoroacetate: A potential acetate analog for prostate tumor imaging—In vivo evaluation of 18F-fluoroacetate versus 11C-acetate. *J Nucl Med* 48:420–428.
30. Uhlén M, et al. (2015) Proteomics. Tissue-based map of the human proteome. *Science* 347:1260419.
31. O JH, Lodge MA, Wahl RL (2016) Practical PERCIST: A simplified guide to PET response criteria in solid tumors 1.0. *Radiology* 280:576–584.
32. Lane MC, Alteri CJ, Smith SN, Mobley HL (2007) Expression of flagella is coincident with uropathogenic Escherichia coli ascension to the upper urinary tract. *Proc Natl Acad Sci USA* 104:16669–16674.
33. Andreu N, et al. (2010) Optimisation of bioluminescent reporters for use with mycobacteria. *PLoS One* 5:e10777.

MEDICAL SCIENCES